Results in Engineering 26 (2025) 105458

Contents lists available at ScienceDirect

Results in Engineering

journal homepage: www.sciencedirect.com/journal/results-in-engineering

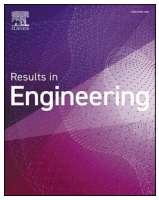

A 3D-printed circularly polarized cavity-based slotted waveguide antenna for kidney cancer detection application

Rashad H. Mahmud [a,b,*], Mustafa M. Mohammed [c], Halgurd N. Awl [d,e], Yadgar I. Abdulkarim [f], Ramin Khosravi [g], Idris H. Salih [b], Majeed Hasan Mahmood [h]

[a] Department of Physics, College of Education, Salahaddin University-Erbil, Erbil, Kurdistan Region 44002, Iraq
[b] Mechatronic Engineering, Faculty of Engineering, Tishk International University, Erbil, Kurdiatn Region 44001, Iraq
[c] Department of Aviation, College of Engineering, Salahaddin University-Erbil, Erbil, Kurdistan Region 44002, Iraq
[d] Department of Communication, Engineering College, Sulaimani Polytechnic University, Sulaimani, Kurdistan Region 46001, Iraq
[e] Faculty of Engineering and Computer Science, Qaiwan International University, Sulaimani, Kurdistan Region, Iraq
[f] Physics Department, College of Science, Charmo University, Chamchamal, Sulaimania, Kurdistan Region 46023, Iraq
[g] Electrical and Computer Engineering Department, University of Alberta, Edmonton, AB T6G 2R3, Canada
[h] Kurdistan Higher Council of Medical Specialties, Erbil, Iraq

ARTICLE INFO

Keywords:
Axial ratio
Cavity resonator
Circularly polarized radiation
Slot antenna
Waveguide technology

ABSTRACT

This paper presents a novel circularly polarized (CP) slot antenna based on a waveguide cavity resonator for kidney cancer detection applications. The cavity is coupled to the input port via a capacitive iris, ensuring strong coupling and improved impedance matching compared to conventional waveguide slot antennas. An L-shaped radiating slot, formed by two orthogonal linearly polarized (LP) slots, is etched into the broad wall of the cavity to generate CP radiation. The axial ratio bandwidth (ARBW) is enhanced by optimizing the slot dimensions. To validate the predicted results, a 3D-printed prototype was fabricated and tested. The measured 10- dB fractional bandwidth (FBW) is 7.4 % at the center frequency (f_0) $f_0 = 10$ GHz, while the 3- dB ARBW and peak gain are 7.0 % and 7.5 dBic, respectively. The detection capability of the proposed antenna is evaluated in a modeled measurement system, revealing a calculated sensitivity of 0.175 GHz/RIU at f_0 =10 GHz. Furthermore, the antenna exhibits a resonance frequency shift of 0.21 GHz when tested with renal cancer cells, distinguishing them from normal cells. These findings demonstrate that the proposed antenna effectively distinguishes between normal and cancerous kidney cells, making its potential as a good candidate for kidney cancer detection.

1. Introduction

In recent years, wireless body area network (WBAN) systems have revolutionized healthcare monitoring by enabling real-time patient data acquisition and facilitating remote diagnosis of abnormal health conditions through biomedical telemetry devices [1–6]. Unlike computed tomography (CT) scans, X-rays, and magnetic resonance imaging (MRI), these devices offer non-invasive, non-ionizing, safe, and portable treatment for continuous health monitoring [4,5,7]. By generating electromagnetic signals, they collect physiological data from deeper organs and transmit it to external units for analysis [7,8]. The effectiveness of biomedical telemetry devices largely depends on the performance of their antennas [9]. Key antenna requirements for such applications include compactness, a low-profile design, wide bandwidth, and a directive radiation pattern [8,10]. To enhance sensing and imaging capabilities, extensive research has focused on ultrawideband (UWB) antennas for wearable and biomedical applications [10–14]. Moreover, to ensure efficient signal transmission through various biological tissues including skin, fat, and muscle, the antenna must exhibit circularly polarized (CP) radiation, thereby minimizing reflections and polarization mismatches with external units.

CP implantable antennas have been designed to operate at 0.915 GHz and 2.45 GHz, enabling efficient wireless power transfer for biomedical applications [15–19]. Additionally, UWB microstrip patch and dielectric resonator antennas, operating within 2.9–7.0 GHz and 6.5–12.5 GHz, have been developed for breast tumor detection [20,21]. For wireless body sensor networks (WBSNs) and health monitoring systems, wearable multiband annular slot antenna and polymer-based

* Corresponding author.
E-mail address: rashad.mahmud@su.edu.krd (R.H. Mahmud).

https://doi.org/10.1016/j.rineng.2025.105458
Received 1 February 2025; Received in revised form 2 May 2025; Accepted 22 May 2025
Available online 25 May 2025

broadband antennas have been proposed, ensuring reliable performance across wide frequency bands [22,23]. Furthermore, dual-polarized antennas utilizing substrate integrated waveguide (SIW) and cavity resonator technologies have been introduced for electromagnetic imaging (EMI) applications [7,24]. In the context of wireless endoscopy and wearable technologies, dual-band and triple-band multiple-input multiple-output (MIMO) antennas based on microstrip structures have been developed, operating at 0.915 GHz and 2.45 GHz and demonstrating high data rate capability [25–27]. Additionally, an equilateral triangular microstrip patch antenna, optimized using Gaussian process regression, was designed to operate at 3.0 GHz, showcasing its potential for microwave imaging applications [28]. To enhance glucose sensing capabilities, multiple slots were incorporated across the width of a microstrip patch antenna, further improving its sensitivity and performance [29].

Recent advancement in biomedical research have led to the development of various antenna-based systems for detecting kidney cancer cells and renal stones. The detection methodology primarily relies on the resonance frequency shift (Δf_0) or change in the reflection coefficient magnitude (ΔS_{11}) when the antenna interacts with normal and renal tissues. These variations arise due to differences in the dielectric properties of normal and renal cells. In [30], a microstrip patch antenna operating within 0.2–0.6 GHz was utilized to identify kidney tumors of six different sizes. However, the observed ΔS_{11} values were relatively small, and the Δf_0 shift was limited to <0.0064 GHz, restricting its sensitivity. Another study employed a microstrip patch antenna resonating at 2.26, 2.38, 2.49, 2.5, and 2.6 GHz in an MEI system for kidney calcium stone detection [31]. The measured ΔS_{11} values at these resonance frequency points were 0.32, 2.2, 1.5, 2.5, and 5 dB, respectively, indicating a small varying sensitivity across the S_{11} response. Additionally, an UWB monopole antenna, operating within 3–11 GHz range, has been introduced for an MWI system to detection kidney stone detection [32]. In this MWI system, water and water-calcium solutions were simulated, achieving a ΔS_{11} value of 12 dB for both substances, demonstrating its potential for high-sensitivity detection.

In this paper, a novel CP antenna based on a TE_{101} mode rectangular waveguide cavity-resonator is proposed for the detection of kidney cancer cells. The input port is coupled to the cavity via a capacitive iris, which enhances impedance matching compared to conventional waveguide slot antennas. The radiating element consists of an L-shaped slot, formed by two unequal orthogonal linearly polarized (LP) slots, etched into the broad wall of the cavity. CP radiation is achieved through the superposition of the orthogonal LP fields generated by these slots. The ARBW is controlled by adjusting the slot dimensions. The antenna's sensitivity and Δf_0 are evaluated in a modeled measurement system. The results indicate that the calculated antenna sensitivity is 0.175 GHz/RIU at f_0 =10 GHz. Furthermore, when a renal cancer cell is tested instead of a normal cell, a Δf_0 of 0.21 GHz is observed, demonstrating the antenna's effectiveness in biomedical diagnosis.

This paper is organized as follows. Section 2 discusses the design concept of both conventional and CP waveguide slot antennas based on a cavity resonator. Section 3 compares the simulated results of a conventional slot antenna with those of the two proposed CP antenna. In Section 4, the detection performance of the proposed CP antennas is analyzed in the presence of both cancerous and normal cells. Section 5 provides details on the fabrication and measurement procedures. Finally, Section 6 concludes the paper with a summary of key findings.

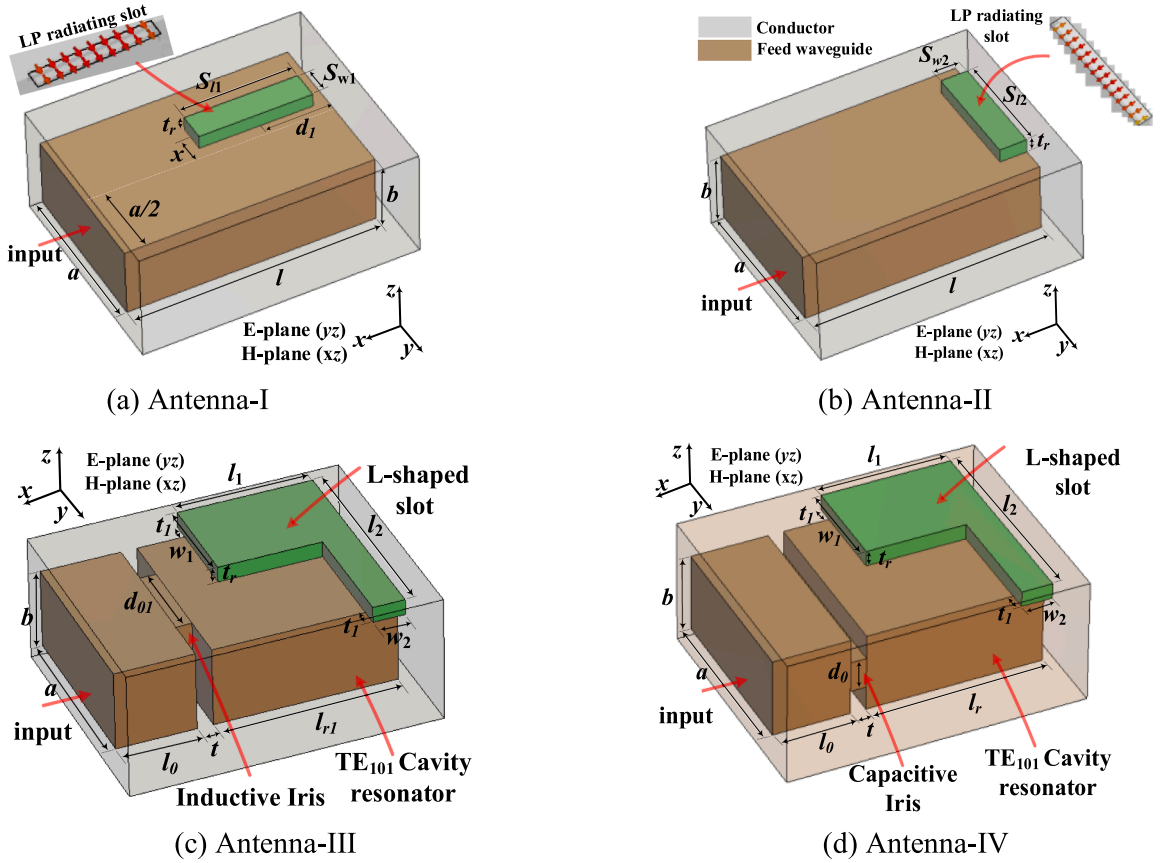

Fig. 1. (a) Horizontal and (b) vertical slotted waveguide antennas. (c) and (d) are the proposed CP antennas based on waveguide cavity-resonator. Dimensions in mm are; l = 30.0, d_1 = 9.35, S_{w1} = 2, S_{l1} = 14.71, t_r = 2.0, b = 10.16, a = 22.86, x = 10.0, S_{w2} = 2, S_{l2} = 14.30, l_0 = 12.0, t = 2, l_r = 22.90, l_{r1} = 16.30, d_0 = 3.4, d_{01} = 13.5, w_1 = 12.1, l_1 = 13.1, w_2 = 3.9, l_2 = 28.0.

2. Theory and design

This section presents the design of the proposed CP waveguide slot antenna, which is based on a rectangular cavity-resonator structure. Antenna-I, illustrated in Fig. 1(a), represents a conventional rectangular waveguide slot antenna. The radiating slot exhibits LP and is displaced from centerline of the broad-wall by a distance (x). This displacement disrupts the surface currents induced by the TE_{10} mode magnetic field on the waveguide walls, thereby exciting the slot [33]. The value of x can be determined using the following relation [34]:

$$g_n = \frac{1}{n} = 2.09\ \frac{\lambda_g}{\lambda_0}\left(\frac{a}{b}\right)\left(cos^2\frac{\pi\lambda_0}{2\lambda_g}\right)\left(sin^2\frac{\pi x}{a}\right) \quad (1)$$

Here g_n is the slot's normalized conductance, n is the slot numbers etched on the broad-wall, and a and b correspond to the broad wall and narrow wall dimensions of the waveguide, respectively. Additionally, λ_0 is free space resonant wavelength, while λ_g is the guided wavelength. For Antenna-I a WR-90 waveguide with dimensions a = 22.86 mm and b = 10.16 mm is utilized. The λ_0 and λ_g are computed at f_0=10 GHz for the TE_{10} mode using the relation in [35], yielding 29.97 mm and 39.70 mm, respectively. The initial x value is determined using Eq. (1) and is found to be approximately 7.17 mm. The slot length (S_{l1}) and width (S_{w1}) can be calculated using the relation given in [34]:

$$2\log\left(\frac{\text{slot length } (S_{l1})}{\text{slot width } (S_{w1})}\right) \gg 1 \quad (2)$$

Elliot in [36] found that for a resonant slot, the length and width can be approximated as S_{l1} =0.464 λ_0 and S_{w1} =0.05 λ_0, respectively. The distance from the slot center to the waveguide end (d_1) is set to a quarter of the guided wavelength (0.25 λ_g) to ensure in-phase reflection of the incident wave, thereby enhancing radiation efficiency.

Antenna-II, illustrated in Fig. 1(b), represents another conventional waveguide slot antenna, where the radiating slot is positioned at the waveguide's end. Similar to Antenna-I, this configuration generates LP radiation pattern. The slot dimensions (S_{l2}, S_{w2}) for Antenna-II are determined using the same calculation methods as described earlier. It is important to note that the initial values of the design parameters x, S_{l1}, S_{w1}, S_{l2}, and S_{w2} are computed without accounting for the waveguide wall thickness (t_r). These parameters undergo further optimization using the computer simulation technology (CST) microwave studio simulator [37] to ensure resonance at 10 GHz and achieve an optimal FBW. The final optimized dimensions are provided in the caption of Fig. 1.

Antenna-III and Antenna-IV, illustrated in Figs. 1(c) and (d), are the proposed CP antennas based on TE_{101} mode rectangular waveguide cavity resonators. Antenna-III utilizes an inductive iris for coupling the cavity to the input port, whereas Antenna-IV employs a capacitive iris. Both designs incorporate an L-shaped radiating slot etched into the broad wall of the cavity, consisting of a pair of unequal orthogonal LP slots. The superposition of the LP fields generates CP radiation without costing extra structure of space. As demonstrated through CST studio simulation and depicted in Fig. 2, the E-field rotates clockwise along the L-shaped radiating slots due to a phase difference at 10 GHz, producing LHCP. The propagation direction is perpendicular to the slot. RHCP can be achieved by repositioning the horizontal slot section (l_1, w_1) to the opposite side. The ARBW is controlled by the slot dimensions (l_1, l_2, w_1, w_2) as discussed in Section 3. The specific dimensions for Antenna-III and Antenna-IV are provided in the caption of Fig. 1.

Fig. 2(b) represents the equivalent circuit of Antenna-IV. The waveguide resonator is assumed to be lossless, represented by parallel lumped L_1 and C_1 elements. A coupling capacitor (C_0) is introduced to account for the capacitive coupling iris between the input port and the cavity, allowing control over the circuit's FBW. The input port waveguide impedance (Z_0) is 500 Ω [35] . The radiation resistance (R_r) represents the power radiated through the L-shaped aperture of Antenna-IV. For optimal impedance matching at the designed frequency f_0=10 GHz, R_r should equal Z_0. The values of L_1 and C_1 can be expressed as a function of (f_0) using the parallel LC relation as follow [35]:

$$f_0 = \frac{1}{2\pi\sqrt{L_1 C_1}} \quad (3)$$

for Antenna-IV, given f_0 =10 GHz and an arbitrarily chosen C_1 of 0.47 pF, the corresponding L_1 value, computed using Eq. (3), is 0.538 nH. The value of C_0 is set to 2.0 pF to ensure strong coupling and achieve the required FBW. The circuit element values found above are inserted into the advanced design system (ADS) simulator to obtain the circuit response as will be presented in Section 3.

3. Simulated results and analysis

Fig. 3(a) compares the simulated S_{11} response and realized gain of Antennas I, II, III, and IV. Among them, Antenna-IV exhibits superior impedance matching at 10 GHz, while Antenna-III achieves a slightly wider 10-dB FBW of 7.6 % compared to Antenna-IV's 7.5 %. This improvement is attributed to the inductive coupling iris used in Antenna-III, which inherently supports a broader bandwidth. However, Antenna-IV achieves the highest peak gain of 7.8 dBic at 10 GHz outperforming the other designs. Fig. 3(b) shows that all antennas achieve simulated total efficiencies exceeding 95 %. Additionally, the AR

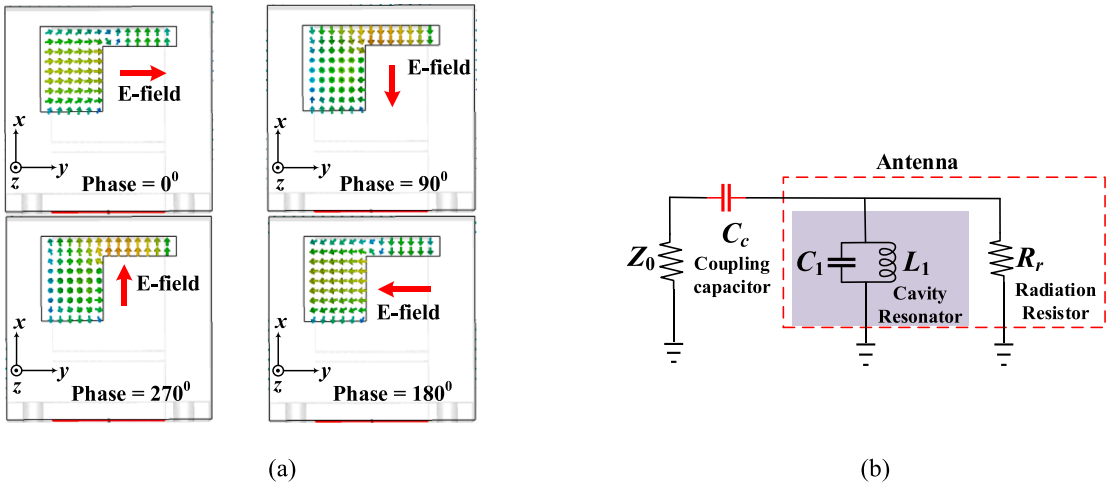

(a) (b)

Fig. 2. E-field rotation with phase change of 0°, 90°, 180°, 270° over the L-shaped radiating slot of Antenna-IV. (b) Equivalent circuit of Antenna-IV. The element values are: Z_0= 500Ω, C_c=2.0 pF, C_1= 0.47 pF, L_1=0.538 nH, R_r= 500Ω.

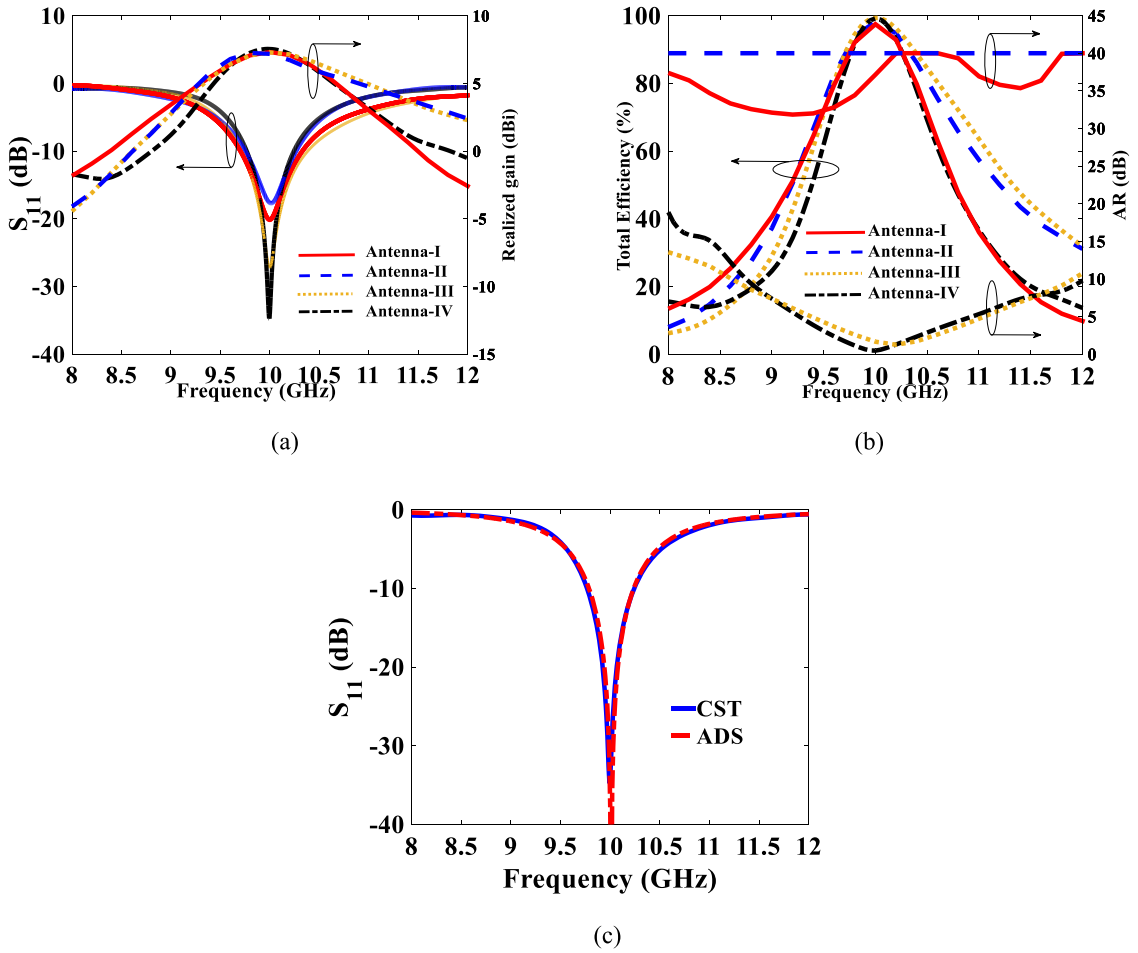

Fig. 3. Simulated (a) S_{11}, realized gain, and (b) Total efficiency versus frequencies of Antennas-I, II, III, and IV. (c) Simulated S_{11} response of Antenna-IV obtained from the equivalent circuit and CST.

variations with frequency are illustrated. Antennas I and II maintain an AR of approximately 40 dB at 10 GHz, indicating linear polarization. In contrast, the L-shaped slots in Antennas III and IV yield AR values below 3 dB at 10 GHz, ensuring CP radiation. Despite their similar performance, Antenna-IV is preferred due to its capacitive coupling iris, which is implemented along the broad wall (a) of the waveguide cavity. This placement enhances the 3D printing device's tolerance. Fig. 3(c) presents the simulated S_{11} response of Antenna-IV, obtained from both the equivalent circuit model and CST simulations. The close agreement between these results confirms the accuracy of the circuit representation.

The effect of dimensions t and d_0 on Antenna-IV's S_{11} response are shown in Figs. 4(a) and (b). As t dimension increases, the incident wave encounters greater difficulty coupling into the cavity, resulting in a degraded S_{11} response and a frequency shift toward lower values. In contrast, increasing d_0 up to 3.5 mm optimizes the capacitive iris as a matching circuit, improving the S_{11} response and aligning it with f_0=10 GHz. Fig. 5 illustrates the impact of L-shaped slot dimensions (l_1, l_2, w_1,

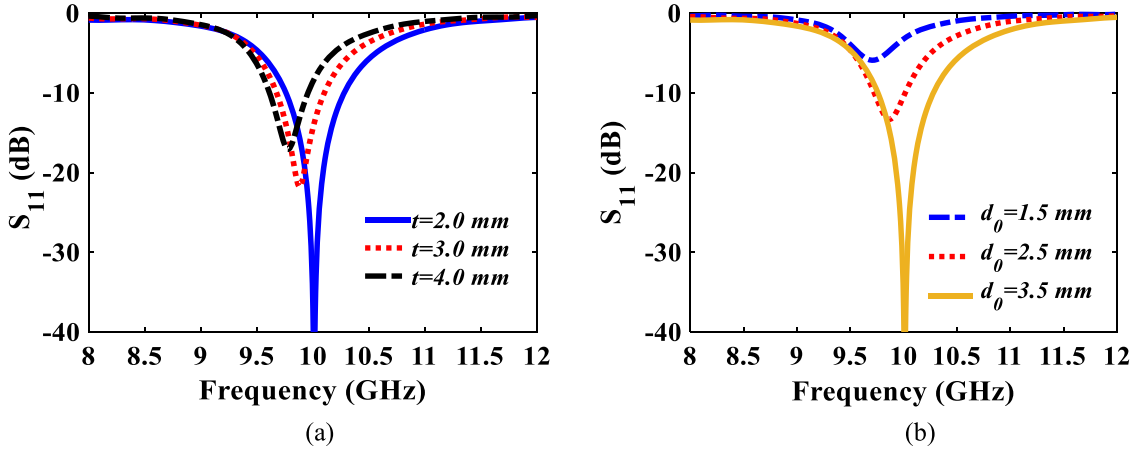

Fig. 4. The S_{11} variation of Antenna-IV under the impact of: (a) t variation when d_0= 3.5 mm, and (b) impact of d_0 dimensions when t = 2.0 mm.

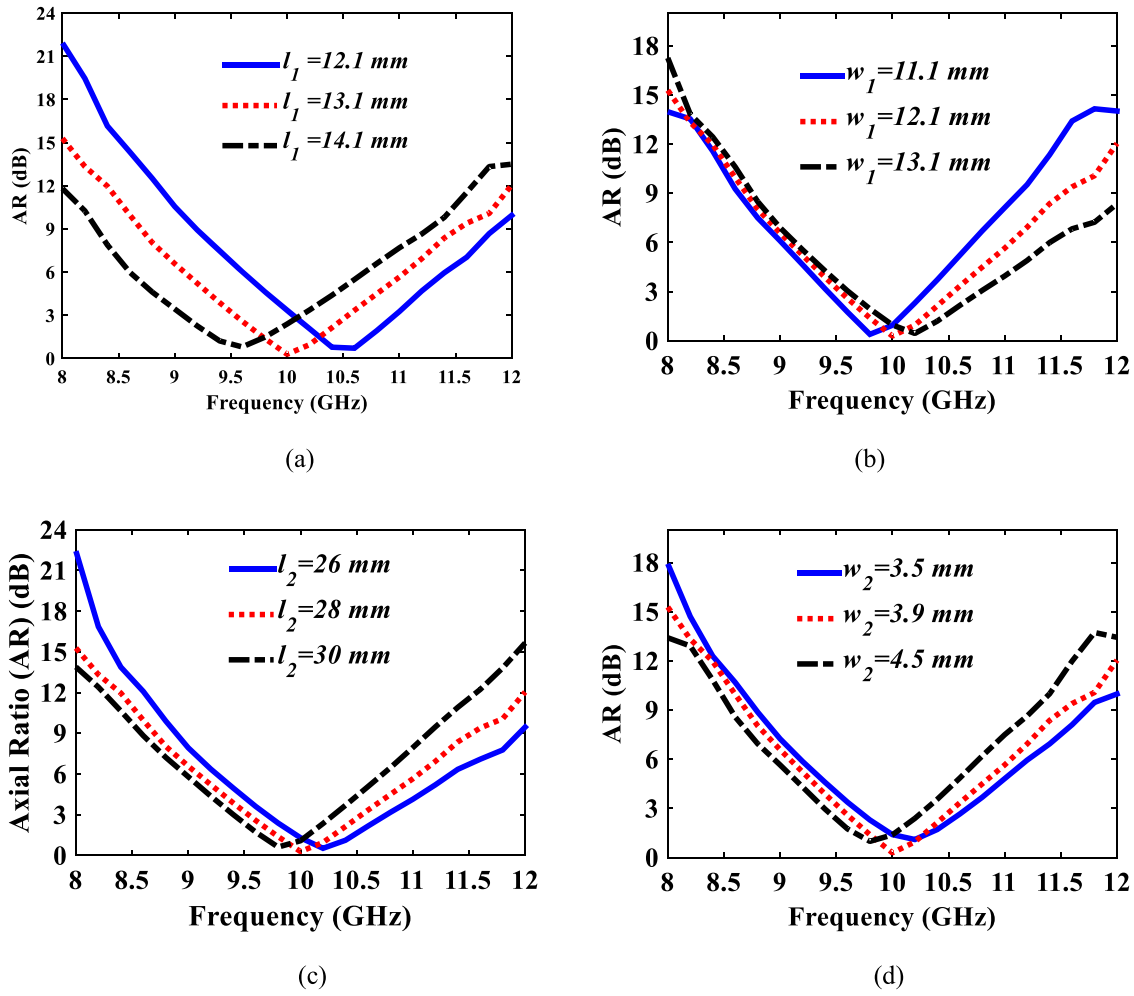

Fig. 5. The influence of the dimensions (a) l_1 when w_1= 12.1 mm, l_2= 28 mm, w_2= 3.9 mm, (b) w_1 when l_1= 13.1 mm, l_2=28 mm, w_2=3.9 mm, (c) l_2 when w_1= 12.1 mm, l_1=13.1 mm, w_2=3.9 mm, and (d) w_2 when w_1= 12.1 mm, l_1=13.1 mm, l_2=28 mm on the AR performance of Antenna-IV.

w_2) on the AR response. The maximum achievable 3- dB ARBW is 7.0 % at $f_0 = 10$ GHz. Additionally, increasing l_1, l_2, and w_1 values shift f_0 of the AR downward, whereas a larger w_2 shifts it upward.

Table 1 compares the radiation characteristics of Antenna-IV with related. The proposed antenna exhibits competitive performance in terms of gain, ARBW, and small size, making it a suitable candidate for cancer detection applications.

4. Sensing performance

This section presents a framework for detecting cancerous renal cells. The proposed detection system, illustrated in Fig. 6*a*, utilizes a one-port reflection coefficient measurement technique [43], where the antenna functions as a microwave sensor. The test sample is prepared by placing it between coverslip layers and positioning it directly on the radiating aperture of the antenna. The antenna is then connected to the vector network analyzer (VNA) and a computer to monitor variations in the S_{11} response (ΔS_{11}) and resonance frequency shift ((Δf_0)) when normal and

Table 1
Performance comparison of Antenna-IV with some other related works.

Refs.	Antenna Type	f_0 (GHz)	Antenna size ($\lambda_0 \times \lambda_0 \times \lambda_0$)	Single element peak gain (dBic)	FBW (%) at S_{11}=−10 dB	3- dB AR (%)	Required extra circuit to produce CP radiation
[38]	Slotted waveguide antenna	14.5	0.74 × 0.82 × 1.44	8.07	3.5	9.0	Yes
[39]	Slotted SIW	10.0	0.35 × 1.07 × 0.1	5.90	3.0	2.0	Yes
[40]	Slotted waveguide antenna	30	3.62 × 2.1 × 0.91	9.80 four slots	6.7	1.2	No
[41]	T-Slotted waveguide antenna	29.5	1.09 × 1.29 × 0.44	6.78	3.4	1.0	No
[42]	Slotted waveguide antenna	4.0	1.30 × 1.30 × 0.85	6.5	11.0	13.3	Yes
This work Antenna-IV	**L-shaped slotted waveguide antenna**	**10.0**	**1.20 × 0.89 × 0.47**	**7.50**	**7.40**	**7.0**	**No**

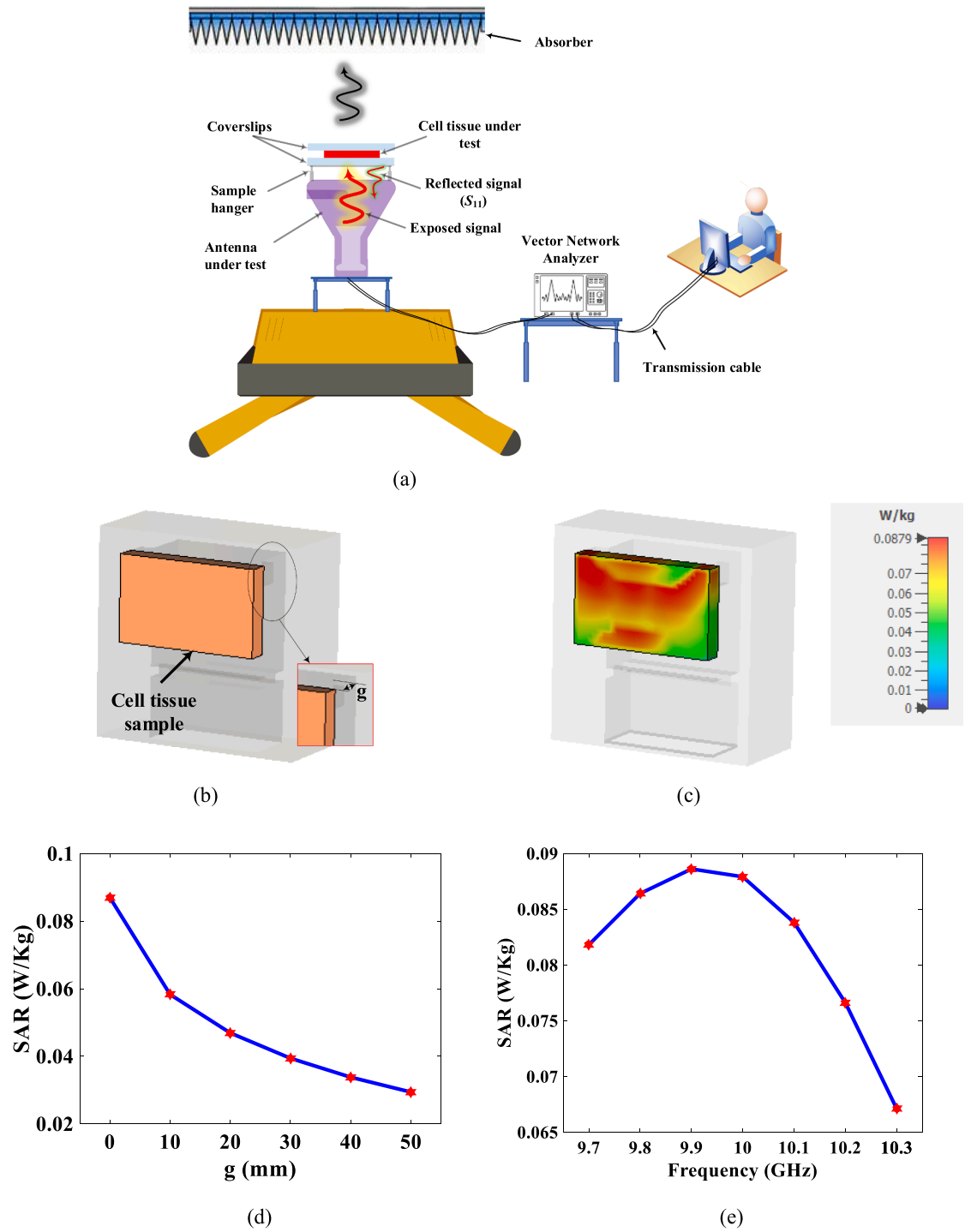

Fig. 6. Proposed detection framework using antenna as a microwave sensor. (b) 1-gram modeled sample under test. (c) SAR distribution on the sample. (d) SAR variation with the change of sample-antenna distance (g). (d) SAR variation with the change of frequency when $g = 0.0$ mm.

cancer cells are introduced. A key advantage of this system is that the human body remains in the farfield region of the antenna's radiation patten, thereby minimizing exposure to electromagnetic waves. To assess the safety of electromagnetic radiation, the Specific Absorption Rate (SAR) is used, which quantifies the amount of electromagnetic energy absorbed by human tissue. SAR is defined as the rate of energy absorption per unit mass and is mathematically expressed as [44]:

$$\mathrm{SAR} = \frac{|E|^2\sigma}{\rho} \tag{4}$$

where E (V/m), σ (S/m), and ρ (Kg/m^3) represent the maximum electric field intensity, tissue electrical conductivity, and tissue mass density, respectively. There are two standards for SAR value calculation. According to IEEE C95.1:1999, the SAR limit for a 1-gram average spatial tissue is 1.6 W/Kg. In IEEE C95.1:2005, this value was updated to 2 W/Kg for a 10-gram average spatial tissue [45,46].

In Fig. 6(b), a normal cell sample is placed directly on the radiating aperture of the antenna ($g = 0.0$ mm). The SAR distribution on the sample, shown in Fig. 6(c), indicates a maximum SAR value of 0.0879 W/Kg for a 1-gram average tissue at 10 GHz, which remains below safety

limits. Additionally, Fig. 6(d) demonstrates a significant decrease in SAR as the distance between the sample and the antenna (g) increases. Furthermore, Fig. 6(e) presents the variation of SAR with changes in the frequency when $g = 0.0$ mm. The results confirm that the SAR value remains below the safety limits across the operating frequency of interest.

The proposed CP antenna was tested within the proposed detection system mentioned above. To evaluate and enhance the antenna's sensitivity, three analyte sections of different shapes were designed and placed on the antenna's radiating aperture, as shown in Figs. 7(a), (b) and (c). The S_{11} results, presented in Fig. 8(a), demonstrate that the square-shaped analyte offers higher sensitivity in terms of Δf_0 and ΔS_{11} value due to its complete coverage of the radiating aperture. The impact of the square-shaped analyte's refractive index (n) on the Δf_0 of the antenna is shown in Fig. 8(b). As the n increases, the f_0 shifts to the lower frequency band. This shift can be used to determine the sensitivity of the antenna [47]. Based on a linear fitting curve in Fig. 8(c), the sensitivity is calculated to be 0.175 GHz/RIU at f_0 =10 GHz, with an R^2 value of 0.9945, indicating a strong linear relationship between n changes and frequency shifts. This strong sensitivity between the refractive index and frequency shift may be attributed to the higher operating frequency of 10 GHz, which allows interaction with fine structures and subtle changes in the dielectric properties of healthy and malignant tissues. Besides, the wavelength of the radiated fields is influenced by changes in the effective permittivity, which is created by changes in the refractive index (RI) surrounding the antenna. As the resonance of the antenna is dependent on its physical dimensions in relation to the wavelength, a shift in RI results in a shift in the resonance frequency. The antenna's sensing capabilities are based on the fact that an increase in RI usually results in a decrease in the resonance frequency because the antenna behaves as though it is electrically longer.

The proposed antenna is further used to diagnose cancerous cells as shown in Fig. 9(a). To ensure error-free results, two coverslip layers are used to sandwich the sample. The test involves placing samples of normal and cancerous renal cells between the coverslips and positioning them on the radiating aperture. The identification process relies on the difference in n value between healthy and cancerous cells, enabling precise characterization based on Δf_0 and ΔS_{11} values. The simplified model of the frequency dependence of n presented in [48] is used to characterize the material of the samples. The refractive index value of normal cells (n_f) is approximately 2.29, while, for renal cancer cells (n_c), it ranges from 2.75 to 2.91 [49]. Also, the relative permittivity of normal renal cells (ε_{rn}) is 5.2441, while it is for cancerous renal cell (ε_{rc}) = 7.5625. Additionally, the other physical properties of normal and renal cancer cells, which are imported into the CST simulator for the detection investigation, are given in the caption of Fig. 9.

The S_{11} response of the antenna, when normal and cancerous cell samples are placed between the coverslip layers, is shown in Fig. 9(b). When a normal cell sample is used, the antenna's f_0 shifts by 0.104 GHz toward the higher frequency band. Both Δf_0 and ΔS_{11} become more pronounced, 0.21 GHz and 3 dB, when a cancerous cell sample is placed on the aperture. These results confirm that the proposed antenna can effectively distinguish between normal and cancerous renal cells.

Further sensing investigations are conducted to study the effects of sample thickness (R_t) and the gap (g) between the radiating aperture and the sample. Fig. 10(a) shows that increasing the g value from 0.0 mm to 2 mm alters the magnitude of S_{11} and reduces the Δf_0 value from 0.20 to 0.1 GHz. This occurs because the propagated EM wave has a higher chance of leaking and scattering away from the sample. Fig. 10(b) demonstrates that the R_t value has a negligible effect on frequency sensitivity, with a Δf_0 value of only 0.006 GHz within the range of 1 mm to 3 mm. However, increasing the R_t value significantly affects the ΔS_{11} magnitude, as thicker sample thickness leads to increased reflection. This is because as the R_t dimension increases, the sample density also increases, making it more resistant to the penetration of the EM wave. The sensing performance of the proposed antenna is compared with those related works reported in the literature, as shown in Table 2. It is evident that the proposed antenna has a strong sensitivity in terms of refractive index, Δf_0, and ΔS_{11}. Additionally, its size is compact and competitive compared to the currently related works, making it a suitable candidate for cancerous cell detection applications.

5. Fabrication and measurement

The proposed Antenna IV was fabricated in two separate parts using 3D printing technology, with a dimensional tolerance of ±50–100 μm, in order to reduce fabrication costs and minimize performance losses, as illustrated in Fig. 11. These pieces were printed using polylactic acid (PLA) polymer and subsequently coated with M.G. chemical shielding spray [51]. While this conductive spray facilitates electrical performance, it may introduce conductivity variations and additional losses in the antenna's response. To mitigate these effects, each piece underwent a double coating process and then assembled using plastic screws to prevent electromagnetic interference. During the coating process, consistent rotation of the prototype was necessary to ensure uniform coverage, particularly inside the slot and along the cavity corners, as inconsistent coating in these regions could result in additional losses. Furthermore, the thickness of the conductive coating must be accounted for during the design stage to ensure it has a negligible effect on the simulated performance. Finally, the surface roughness is a critical parameter influencing the measured response; therefore, the surface must be sufficiently smooth to reduce discrepancies between simulated and experimental results.

The S_{11} and realized gain are measured in an anechoic chamber room. Fig. 12(a) shows good agreement between the measured and simulated S_{11} responses across the entire operating frequency band. A slight shift in the measured S_{11} towards the lower frequency band is observed, with a 10- dB FBW of 7.4 % at 10 GHz, slightly narrower than the simulated result. These differences are attributed to fabrication tolerances. The realized gain is measured using the gain-transfer method [52], with a broadband horn antenna used as a reference antenna. At 10 GHz, the measured gain is 7.5 dBic, slightly lower than the simulated

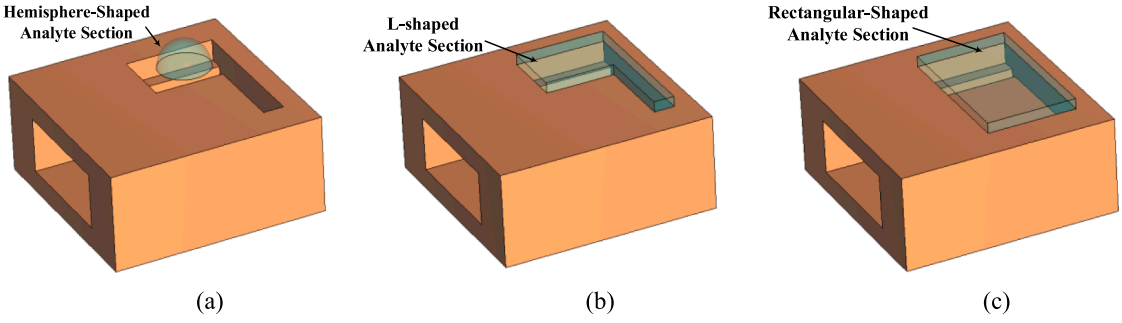

Fig. 7. The antenna with the presence of a) hemisphere, b) L-shaped, and c) rectangular-shaped analyte.

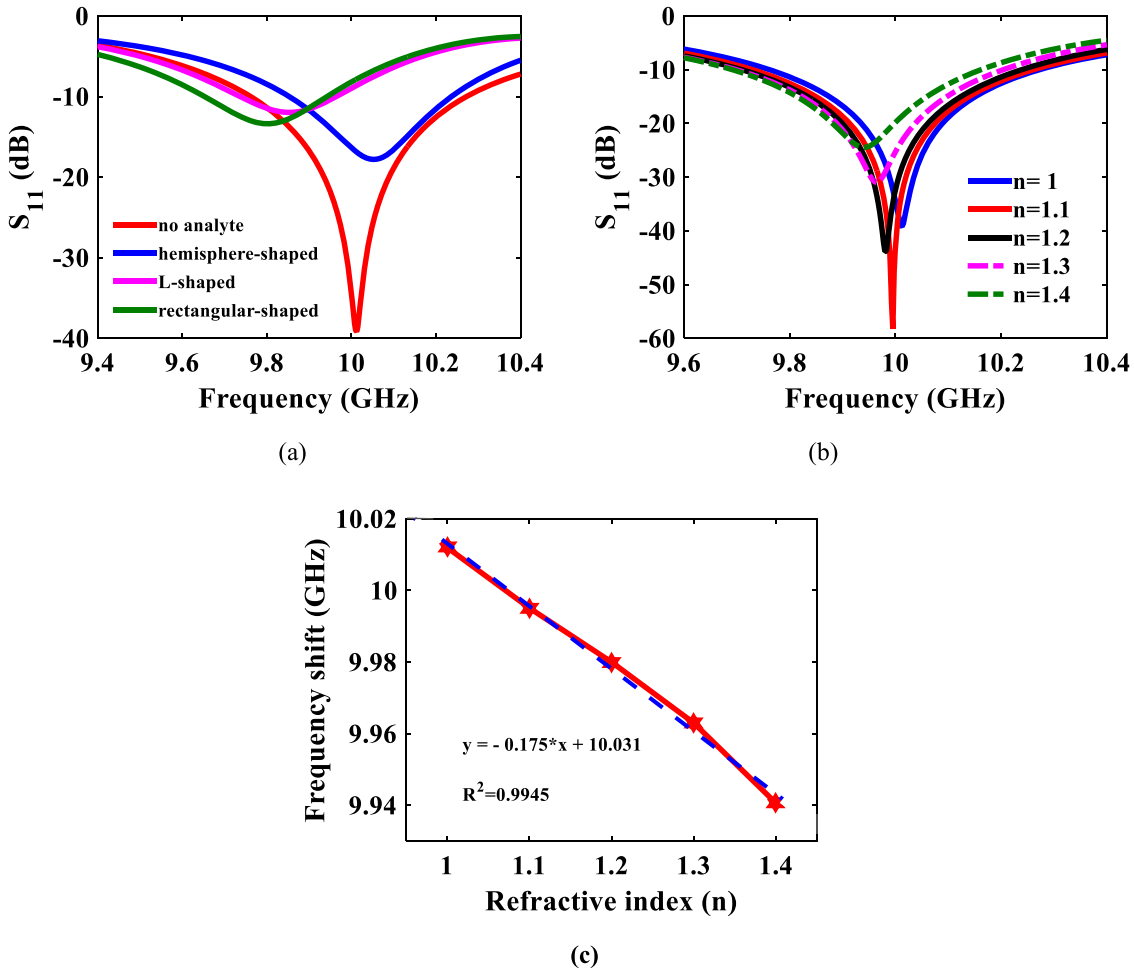

Fig. 8. (a) The simulated S_{11} responses under the influence of three analytes. (b) Impact of n value on S_{11} response. (c) Variation of n value of square-shaped analyte with the resonance frequency shift.

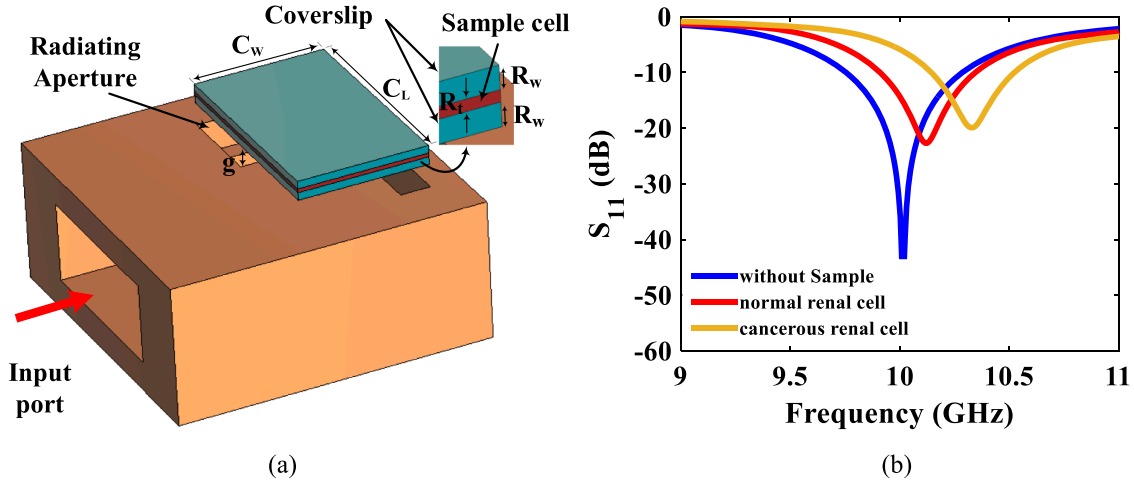

Fig. 9. (a) Antenna setup for cancer cell diagnoses. (b) S_{11} response of the antenna with and without normal and cancerous sample cells. The dimensions in mm are: C_w=17.0, C_L=28.0, R_w=1.0, R_t=0.5, g = 1.0. n_f =2.29, n_c=2.85. n_f =2.29, n_c=2.85. ε_{rn} = 5.2441, ε_{rc} = 7.5625.

value. The measured AR and total efficiency are compared with their simulated ones in Fig. 12(b). The measured AR and total efficiency are compared with the simulated ones in Fig. 12(b), showing a measured 3-dB ARBW of approximately 7.0 % at 10 GHz. The total efficiency is measured in this work from the ratio of the measured realized gain and the simulated directivity. The measured total efficiency is around 90 % within the operating frequency band, which is 5.0 % lower than the simulated efficiency. This reduction is likely due to the conductivity of the M.G. spray conductivity and minor electromagnetic leakage caused by imperfect joints between the antenna parts.

The measured radiation patterns of Antenna-IV are compared with the simulation results in Fig. 13. The difference between the co- (LHCP)

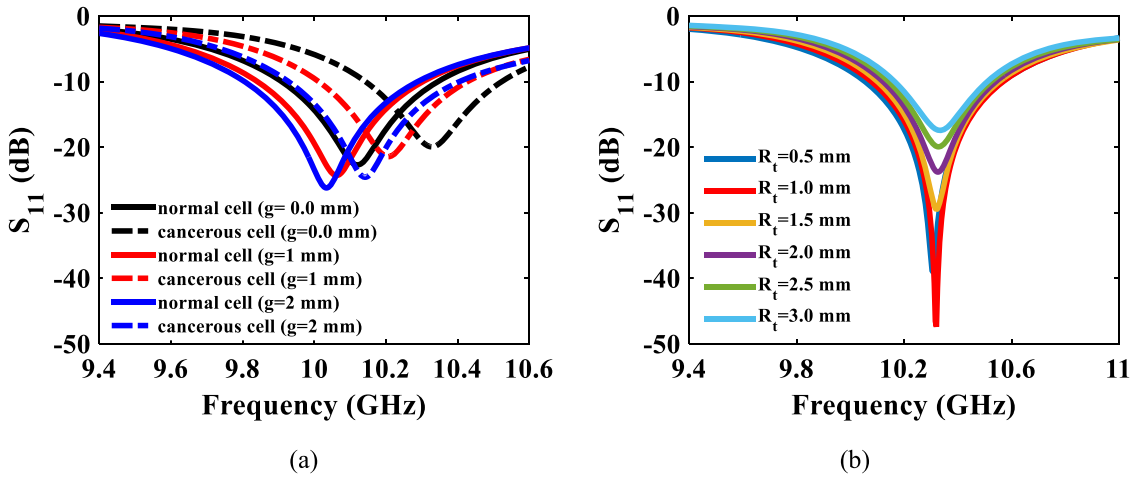

Fig. 10. Impacts of (a) spacing (g), and (b) sample thickness (R_t) dimensions on the S_{11} response of the antenna.

Table 2
Sensing performance of Antenna-IV compared with some other related works.

Refs.	Antenna Type	f_0 (GHz)	Antenna size (*$\lambda_0 \times \lambda_0 \times \lambda_0$)	Sensitivity (GHz/RIU)	Δf_0 (GHz)	ΔS_{11} (dB)
[30]	Spiral microstrip antenna	0.4	27.5 × 15 × 4.75	*NG	NG	Too small
[31]	Microstrip patch antenna	2.4	NG	NG	NG	1.25
[32]	Monopole Antenna	7.0	2.5 × 2.5 × 0.11	NG	NG	12
[50]	Monopole Antenna	0.4032	34.72 × 24.8 × 2.0	NG	0.011	NG
[44]	Microstrip patch antenna	2.4	83.3 × 32.5 × 0.625	NG	0.028	16.6
This work	**L-shaped slotted waveguide antenna**	**10.0**	**1.20 × 0.89 × 0.47**	**0.175**	**0.21**	**3.0**

* NG: not given. *λ_0 is resonance free space wavelength.

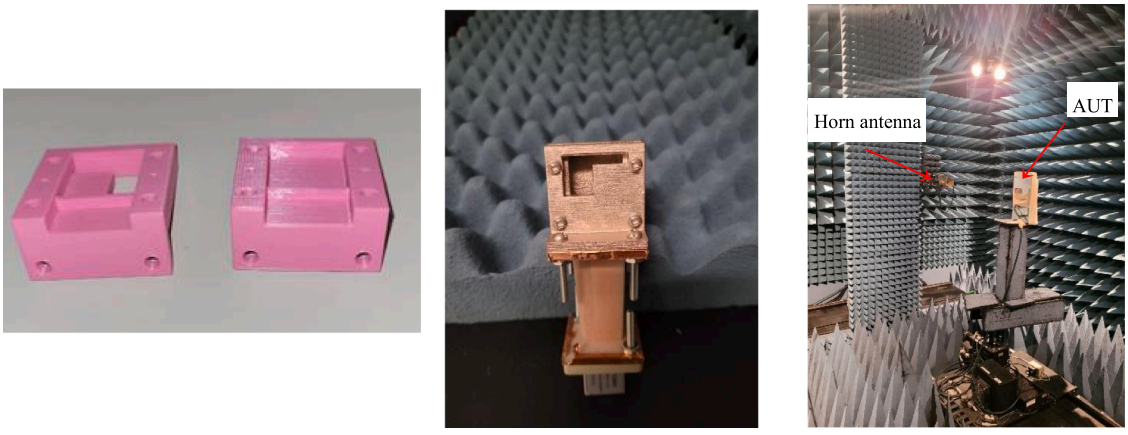

Fig. 11. (a) 3D printing pieces, (b) photograph of Antenna-IV and (c) Antenna-IV under test.

and cross- (RHCP) polarization magnitudes is maximum at broadside as expected. The LHCP main beam remains constant in the normal direction for both of the planes. The side lobe level is below −10 dB over the entire operating frequency band. Discrepancies in the backside lobes are attributed to the connection of a waveguide adaptor during measurement, which was not considered in the simulations. RHCP pattern levels are better than −25 dB in the E-plane but are slightly higher at just below -10 dB in the H-plane. The presence of side lobes in the H-plane measured pattern is likely due to the waveguide adaptor affecting the input port connection.

6. Conclusions

A novel design of a CP slot antenna based on TE_{101} mode rectangular waveguide cavity-resonators has been designed and fabricated using 3D printing technology. The antenna features an L-shaped radiating slot on the broad-wall of the cavity, formed by combining two orthogonal LP slots. The superposition of the LP fields generates CP radiation. The slot dimensions were carefully optimized to achieve a minimum AR value at 10 GHz and broaden the 3- dB ARBW. Measurements of antenna's radiation characteristics validated the simulated results, demonstrating a 10-dB FBW of 7.4 %, a 3-dB ARBW of 7.0 %, and a realized gain of 7.5 dBic at 10 GHz. The performance of the proposed CP antenna is competitive compared to similar related designs and shows promising

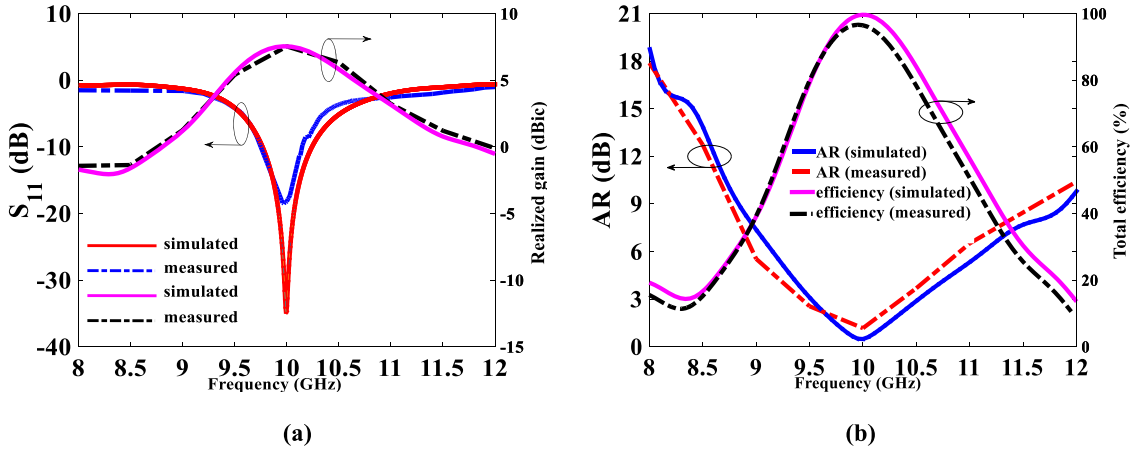

Fig. 12. Measured (a) S_{11} and realized gain, (b) AR, and total efficiency compared with the simulated results.

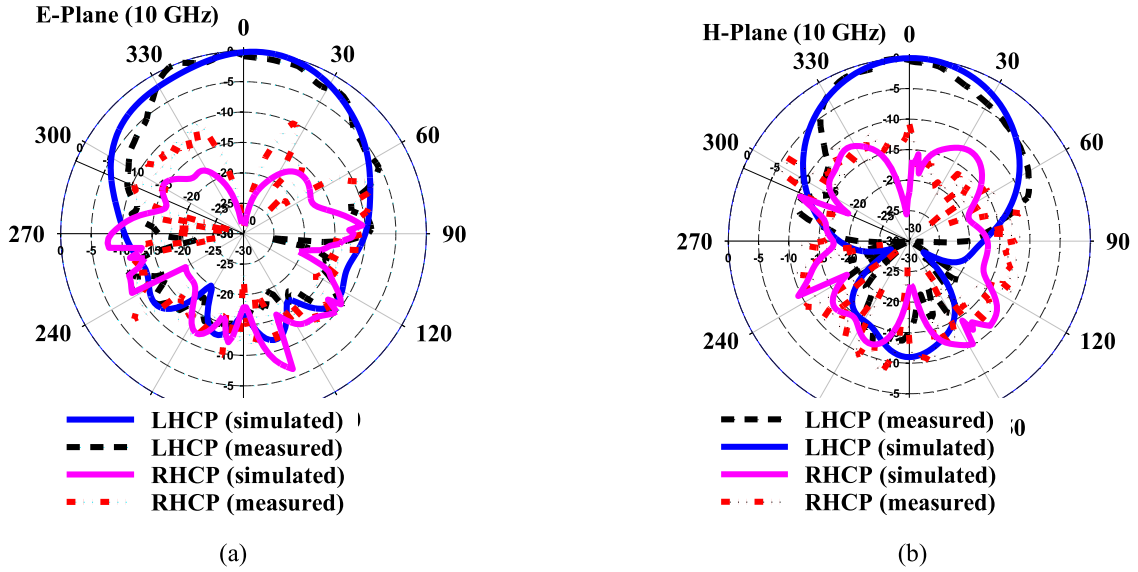

Fig. 13. Measured and simulated Co- and Cross- polarized radiation patterns for both the (a) E-plane, and (b)—H-plane at 10 GHz.

potential for applications in cancer detection systems.

Funding

This work was partially supported by the Intelligent Wireless Technology (IWT) Lab, University of Alberta. Canada, and Salahaddin University-Erbil.

Code availability

Not applicable.

Ethics approval

Not applicable.

Consent to participate

Informed consent was obtained from all authors.

Consent for publication

The authors confirm that there is informed consent to the publication of the data contained in the article.

CRediT authorship contribution statement

Rashad H. Mahmud: Writing – review & editing, Writing – original draft, Validation, Supervision, Software, Resources, Project administration, Methodology, Investigation, Formal analysis, Data curation, Conceptualization. **Mustafa M. Mohammed:** Writing – review & editing, Validation, Resources. **Halgurd N. Awl:** Writing – review & editing, Writing – original draft, Visualization, Validation, Investigation, Formal analysis, Data curation, Conceptualization. **Yadgar I. Abdulkarim:** Writing – review & editing, Validation, Funding acquisition, Data curation. **Ramin Khosravi:** Validation, Resources, Funding acquisition. **Idris H. Salih:** Writing – review & editing, Funding acquisition. **Majeed Hasan Mahmood:** Writing – review & editing, Investigation, Funding acquisition, Conceptualization.

Declaration of competing interest

The authors declare that they have no known competing financial interests or personal relationships that could have appeared to influence the work reported in this paper.

Acknowledgement

The authors would like to thank the Intelligent Wireless Technology (IWT) Lab at the University of Alberta, Canada for fabricating the proposed devices.

Data availability

Data will be made available on request.

References

[1] A.F. Demir, et al., Anatomical region-specific in vivo wireless communication channel characterization, IEEE J. Biomed. Health Inf. 21 (5) (2016) 1254–1262.
[2] X.-T. Yang, H. Wong, J. Xiang, Polarization reconfigurable planar inverted-F antenna for implantable telemetry applications, IEEE Access 7 (2019) 141900–141909.
[3] Y. Liao, M.S. Leeson, M.D. Higgins, C. Bai, Analysis of in-to-out wireless body area network systems: towards QoS-aware health internet of things applications, Electronics 5 (3) (2016) 38.
[4] K.S. Sultan, B. Mohammed, M. Manoufali, A. Mahmoud, P.C. Mills, A. Abbosh, Feasibility of electromagnetic knee imaging verified on ex-vivo pig knees, IEEE Trans. Biomed. Eng. 69 (5) (2021) 1651–1662.
[5] K.S. Sultan, B. Mohammed, M. Manoufali, A.M. Abbosh, Portable electromagnetic knee imaging system, IEEE Trans. Antennas. Propag. 69 (10) (2021) 6824–6837.
[6] M. El Atrash, M.A. Abdalla, H.M. Elhennawy, A wearable dual-band low profile high gain low SAR antenna AMC-backed for WBAN applications, IEEE Trans. Antennas. Propag. 67 (10) (2019) 6378–6388.
[7] S.M.H. Mousavi, M. Moosazadeh, L. Guo, A.M. Abbosh, Compact dual-polarized cavity-backed antenna with wideband performance for deep torso imaging, IEEE Trans. Antennas. Propag. (2024).
[8] Y.A. Kamel, H.A. Mohamed, H. ELsadek, H.M. ELhennawy, Miniaturized triple-band circular-polarized implantable patch antenna for bio-telemetry applications, IEEE Antennas. Wirel. Propag. Lett. 22 (1) (2022) 74–78.
[9] T. Saeidi, S.N. Mahmood, S. Saleh, N. Timmons, A.J.A. Al-Gburi, F. Razzaz, Ultra-wideband (UWB) antennas for breast cancer detection with microwave imaging: a review, Results Eng. (2025) 104167.
[10] S. Saleh, T. Saeidi, N. Timmons, B. Alali, F. Razzaz, A.A. Althuwayb, Compact ultra-wide band two element vivaldi non-uniform slot MIMO antenna for body-centric applications, Results Eng. 24 (2024) 102839.
[11] A. Mohan, N. Kumar, An ultra–wideband compact meander line antenna for brain implants and biotelemetry applications in the 2.45 GHz ISM band, Results Eng. 24 (2024) 103345.
[12] D.M. John, S. Vincent, S. Pathan, K.M. Nayak, T. Ali, A wideband highly flexible CPW-fed antenna based on characteristic mode analysis for 5G wireless wearable sensor applications, Results Eng. 23 (2024) 102412.
[13] V.K. Jhunjhunwala, et al., A four port flexible UWB MIMO antenna with enhanced isolation for wearable applications, Results Eng. 24 (2024) 103147.
[14] S. Saleh, T. Saeidi, N. Timmons, B. Alali, F. Razzaz, A.A. Althuwayb, High-performance UWB Vivaldi Antenna on FR4: a cost-effective solution for wearable technologies, Results Eng. (2025) 104230.
[15] C. Liu, Y. Zhang, X. Liu, Circularly polarized implantable antenna for 915 MHz ISM-band far-field wireless power transmission, IEEE Antennas. Wirel. Propag. Lett. 17 (3) (2018) 373–376.
[16] H. Li, Y.X. Guo, S.Q. Xiao, Broadband circularly polarised implantable antenna for biomedical applications, Electron.Electron .Lett. 52 (7) (2016) 504–506.
[17] Z. Xia, H. Li, Z. Lee, S. Xiao, W. Shao, X. Ding, A wideband circularly polarized implantable patch antenna for ISM band biomedical applications, IEEE Trans. Antennas. Propag. 68 (3) (2019) 2399–2404.
[18] Z.-J. Yang, S.-Q. Xiao, L. Zhu, B.-Z. Wang, H.-L. Tu, A circularly polarized implantable antenna for 2.4-GHz ISM band biomedical applications, IEEE Antennas. Wirel. Propag. Lett. 16 (2017) 2554–2557.
[19] R. Li, Y.-X. Guo, B. Zhang, G. Du, A miniaturized circularly polarized implantable annular-ring antenna, IEEE Antennas. Wirel. Propag. Lett. 16 (2017) 2566–2569.
[20] A. Raza, M.I. Souza, M. Liaqat, V.M. Pepino, B.-H.V. Borges, Ultra-wideband Patch Antenna With Inhomogeneous Artificial Magnetic Conductor and Nearly Constant Radiation Pattern For Breast Tumor Detection, IEEE Antennas and Wireless Propagation Letters, 2024.
[21] A. Gupta, S.K. Yadav, V. Kuamr, M.H. Alsharif, P. Uthansakul, M. Uthansakul, Enhanced breast tumor localization with DRA antenna backscattering and GPR algorithm in microwave imaging, Results Eng. 24 (2024) 103044.
[22] C. Zhang, Z. Zhao, P. Xiao, Q. Liu, N. Wang, G. Li, A miniaturized wearable annular slot antenna based on designer LSPs for telemedicine communication, IEEE Trans. Antennas. Propag. (2024).
[23] M. Hussain, W.A. Awan, S.M. Abbas, Y. Zhu, Design and development of low-profile polymer based broadband antenna for on-body applications, Results Eng. 25 (2025) 103818.
[24] K. Sultan, A. Abbosh, On-body cavity-backed slot antenna with pattern and polarization diversity for medical imaging, IEEE Trans. Antennas. Propag. (2024).
[25] A. Iqbal, S.H. Kiani, M. Al-Hasan, I.B. Mabrouk, T.A. Denidni, A compact dual-band implantable mimo antenna for wireless capsule endoscopy, IEEE Trans. Antennas. Propag. (2024).
[26] R.N. Tiwari, et al., A low-profile dual-band millimeter wave patch antenna for high-speed wearable and biomedical applications, Results Eng. 24 (2024) 103212.
[27] R.N. Tiwari, et al., Triple band lateral 4-port flexible MIMO antenna for millimeter wave applications at 24/28/38 GHz, Results Eng. (2025) 104678, https://doi.org/10.1016/j.rineng.2025.104678, 2025/03/19/.
[28] M.B. Bicer, E.A. Aydin, Analyzing equilateral triangle compact microstrip antennas using gaussian process regression for telemedicine and mobile biomedical imaging systems, Multimed. Tools Appl. 83 (8) (2024) 24435–24465.
[29] S. Todi, P. Agarwal, Sensitivity Analysis of Microstrip Patch Antenna Genres: Slotted and Through-Hole Microstrip Patch Antenna, Biomedical Engineering Letters, 2024, pp. 1–12.
[30] M. Hassan, A. Allam, Effect of kidney malignant tissues on antenna resonance, Universal J. Biomed. Eng. 2 (1) (2014) 1–4.
[31] M. Alwan, S. Sadek, Investigation of Kidney stone using a microstrip patch antenna scanning system, J. Diagnost. 3 (1) (2016) 1–10.
[32] A.J.A. Al-Gburi, I. Ibrahim, Z. Zakaria, A miniature raspberry shaped UWB monopole antenna based on microwave imaging scanning technique for kidney stone early detection, Int. J. Psychosoc. Rehabil. 24 (2) (2020) 1755–1763.
[33] J.L. Volakis, J.L. Volakis, Antenna Engineering Handbook, McGraw-hill New York, 2007.
[34] A. Stevenson, Theory of slots in rectangular wave-guides, J. Appl. Phys. 19 (1) (1948) 24–38.
[35] D.M. Pozar, Microwave Engineering, John wiley & sons, 2011.
[36] R. Elliott, L. Kurtz, The design of small slot arrays, IEEE Trans. Antennas. Propag. 26 (2) (1978) 214–219.
[37] C.M. Studio, CST Microwave Studio, CST Studio Suite, 2008.
[38] R.V. Gatti, R. Rossi, A dual-polarization slotted waveguide array antenna with polarization-tracking capability and reduced sidelobe level, IEEE Trans. Antennas. Propag. 64 (4) (2016) 1567–1572.
[39] L. Lu, Y.-C. Jiao, Z.-B. Weng, H. Zhang, C.-Y. Cui, Design of low-sidelobe circularly polarized loop linear array fed by the slotted SIW, IEEE Antennas. Wirel. Propag. Lett. 16 (2016) 537–540.
[40] X. Wu, F. Yang, F. Xu, J. Zhou, Circularly polarized waveguide antenna with dual pairs of radiation slots at ka-band, IEEE Antennas. Wirel. Propag. Lett. 16 (2017) 2947–2950.
[41] K.C. Dimitrov, Y. Lee, B.-W. Min, J. Park, J. Jeong, H.-J. Kim, Circularly polarized T-shaped slot waveguide array antenna for satellite communications, IEEE Antennas. Wirel. Propag. Lett. 19 (2) (2019) 317–321.
[42] R.-S. Chen, G.-L. Huang, S.-W. Wong, M.K.T. Al-Nuaimi, K.-W. Tam, W.-W. Choi, Bandwidth-enhanced circularly polarized slot antenna and array under two pairs of degenerate modes in a single resonant cavity, IEEE Antennas. Wirel. Propag. Lett. 22 (2) (2022) 288–292.
[43] M.J. Lancaster, "Passive microwave device applications of high-temperature superconductors," *(No Title)*, 1997.
[44] D.A. Saleeb, R.M. Helmy, N.F. Areed, M. Marey, K.M. Almustafa, A.S. Elkorany, Detection of kidney cancer using circularly polarized patch antenna array, IEEE Access 10 (2022) 78102–78113.
[45] B. Kumkhet, et al., SAR reduction using dual band EBG method based on MIMO wearable antenna for WBAN applications, AEU-Int. J. Electron. Commun. 160 (2023) 154525.
[46] I. Safety, IEEE standard for safety levels with respect to Human exposure to electric, magnetic, and electromagnetic fields, 0 hz to 300 GHz, IEEE Std C95 (2019) 1–2019 *(Revision of IEEE Std C95. 1–2005/Incorporates IEEE Std C95. 1–2019/Cor 1–2019)*, pp. 1-312.
[47] S. Niknam, M. Yazdi, S. Behboudi Amlashi, Enhanced ultra-sensitive metamaterial resonance sensor based on double corrugated metal stripe for terahertz sensing, Sci. Rep. 9 (1) (2019) 7516.
[48] B.E. Saleh, M.C. Teich, Fundamentals of Photonics, Wiley New York, 2008.
[49] J. Bai, Y. Shi, C. Liu, S. Wang, W. Xu, S. Chang, Hydrophobic terahertz metamaterial absorber sensor for renal cancer detection application, Opt . Commun. 569 (2024) 130860.
[50] A. Bouazizi, G. Zaibi, A. Iqbal, A. Basir, M. Samet, A. Kachouri, A miniaturized implantable monopole antenna design for kidney cancer detection, World J. Model. Simul. 16 (1) (2020) 3–10.
[51] M.G.C. Manufacturer, M. G. Chemical conductive spray coating, accessed 10/10/2023, https://mgchemicals.com/, 2023. accessed 10/10/2023.
[52] K. Konstantinidis, A.P. Feresidis, P.S. Hall, Multilayer partially reflective surfaces for broadband Fabry-Perot cavity antennas, IEEE Trans. Antennas Propag. 62 (7) (2014) 3474–3481.